



Title	Surface cracking on 3, 9 CSL and random grain boundaries in helium implanted 316L austenitic stainless steel
Author(s)	Sakaguchi, N.; Ohguchi, Y.; Shibayama, T.; Watanabe, S.; Kinoshita, H.
Citation	Journal of Nuclear Materials, 432(1-3), 23-27 https://doi.org/10.1016/j.jnucmat.2012.08.019
Issue Date	2013-01
Doc URL	http://hdl.handle.net/2115/52690
Type	article (author version)
File Information	JNM-D-12-00519-2.pdf



[Instructions for use](#)

Surface Cracking on $\Sigma 3$, $\Sigma 9$ CSL and Random Grain Boundaries in Helium Implanted 316L

Austenitic Stainless Steel

N. Sakaguchi ^{a,*}, Y. Ohguchi ^a, T. Shibayama ^a, S. Watanabe ^a, H. Kinoshita ^b

^aCenter for Advanced Research of Energy and Materials, Faculty of Engineering, Hokkaido

University, Sapporo 060-8628, Hokkaido, Japan

^bFukushima National College of Technology, Iwaki 970-8034, Fukushima, Japan

*Corresponding Author

TEL: +81-011-706-6768, FAX: +81-011-706-6768

E-mail: sakaguchi@eng.hokudai.ac.jp

Present address: CAREM, Faculty of Engineering, Hokkaido University, Kita-13, Nishi-8, Kita-ku,

Sapporo 060-8628, Hokkaido, Japan

Abstract

The relationship between surface cracking at grain boundaries and the grain boundary nature in helium implanted 316L austenitic stainless steel was investigated by *in-situ* annealing in a high-voltage electron microscope, and by SEM and TEM observations. The nucleation and growth of helium bubbles at a random grain boundary was observed during annealing up to 973 K. After annealing, surface cracking was observed at the random grain boundaries and some coincidence site lattice (CSL) boundaries because of the formation and rupture of the helium bubbles at these grain boundaries. At the faceted CSL boundaries, surface cracking occurred only on one boundary facet plane. This indicates that the twin boundary and pure tilt $\Sigma 9$ CSL boundary show the highest resistance to cracking because of their low boundary energies.

Key words

Surface cracking, helium bubble, coincidence site lattice, grain boundary nature, grain boundary faceting

1. Introduction

Helium embrittlement or cracking is one of the major problems associated with the structural and core materials used in fission and fusion reactors. In austenitic stainless steel subjected to intense neutron exposure, a large amount of helium (a few appm in light-water reactor and several hundred appm in fusion reactor) is produced by (n, α) reaction. Usually, helium atoms are insoluble in metal and tend to precipitate as helium bubbles. This occurs preferentially at the grain boundaries. At elevated temperatures, the helium bubbles grow rapidly resulting in weakening of the grain boundaries [1-3]. Under the influence of tensile stress, the formation of helium bubbles leads to intergranular fracture, so-called helium embrittlement [4, 5]. Furthermore, heat-affected zone (HAZ) cracking is a serious problem encountered upon repairing structural and core materials containing high concentrations of helium [6-8]. Welding generates high temperatures and tensile stresses which facilitate the growth of helium bubbles at the grain boundaries [9, 10], leading to helium cracking within the HAZ. It is necessary to suppress helium embrittlement and cracking during welding in helium-containing nuclear reactor materials.

To date, it has been shown that the important processes occurring at grain boundaries such as grain boundary cracking [11], sliding [12], segregation and precipitation [13, 14], and corrosion [15, 16] depend critically upon the nature of the grain boundary. It is generally accepted that low energy grain boundaries, such as small angle boundaries and coincidence site lattice (CSL) boundaries,

unlike high energy random grain boundaries, are highly resistant to grain boundary deterioration. Accordingly, a treatment called grain boundary engineering (GBE) has been developed [17-22]. The GBE treatment is categorized as a thermomechanical treatment that can significantly improve the material properties. It has been reported that a network of random grain boundaries is completely disrupted after GBE processing in austenitic stainless steel, and that the CSL frequency can exceed 80 % [23]. Moreover, improvement of creep resistance [22] and the grain boundary corrosion properties [23] can also be achieved using the GBE treatment.

To evaluate the efficacy of the GBE treatment for overcoming the aforementioned helium embrittlement problems, we have investigated the behavior of surface cracking on grain boundaries in helium ion implanted 316L stainless steel by *in-situ* annealing in a multi-beam high voltage electron microscope (MBHVEM) and by transmission- and scanning electron microscopy (TEM and SEM) observations. The relationship between surface cracking and the nature of the grain boundary is discussed. Particular attention was given to the surface cracking behavior at random grain boundaries and the $\Sigma 3$ and $\Sigma 9$ CSL boundaries.

2. Experimental procedure

2.1 Sample preparation

The composition of the type-316L austenitic stainless steel is given in Table 1. To enhance the

density of $\Sigma 3$ and $\Sigma 9$ CSL boundaries, the samples were prepared using a thermomechanical treatment, in which annealing was conducted at 1323 K for 30 minutes followed by 3 % cold rolling at room temperature and heating at 1260 K for 72 hours. Electron backscatter diffraction (EBSD) patterns were acquired using a field-emission scanning electron microscope (FE-SEM; JEOL JSM-7001FA) equipped with an EBSD instrument (TSL Solutions OIM System 6) to confirm the CSL boundary frequency in the samples. The total CSL frequency ($\Sigma \leq 29$) was measured to be 54 % in the as-received 316L stainless steel, whereas the total CSL frequency increased significantly to 77 % by using the thermomechanical treatment. The individual CSL frequencies increased from 42 % to 57 % as for the $\Sigma 3$ CSL boundary and from 3 % to 9 % as for the $\Sigma 9$ CSL boundary. The samples were then mechanically polished to a thickness of 0.15 mm. The foil samples were punched out onto TEM disks of 3 mm diameter and electropolished in a 5 % HClO_4 + 95 % CH_3COOH solution.

2.2 Helium ion implantation

Helium was implanted in the foil samples using a multi-beam high-voltage electron microscope (MBHVEM; JEOL-JEM-ARM-1300) equipped with 300 kV and 400 kV ion accelerators. The He^+ ions with acceleration energies of 50 kV were implanted at a dose of 1.3×10^{15} ions/cm² at room temperature. The concentration profile of the implanted helium calculated by SRIM software [24] is shown in Fig. 1. The calculated peak concentration of the helium was 1000 appm at a depth of 200

nm.

2.3 Annealing and electron microscopy

The helium ion implanted samples were annealed in the MBHVEM at temperatures up to 973 K for 45 minutes. *In situ* observation of the microstructural changes during heating was carried out using a digital video recorder attached to the MBHVEM. After annealing, the surface morphology of the samples and the distribution of the different types of grain boundary were analyzed using the FE-SEM. Thin foils for TEM analysis were picked up from the sample using the FIB sampling technique, and the foils were then observed with an FEG-TEM (JEOL JEM-2010F).

3. Results

Fig. 2 shows the helium bubble formation behavior in helium ion implanted 316L steel during the *in-situ* heating experiment in the MBHVEM. Before heating, no helium bubbles were seen at the random grain boundary, twin boundary or in the matrix. When the sample temperature reached 773 K, tiny helium bubbles (~10 nm) formed exclusively at the random grain boundary. The bubbles grew slowly upon further heating of the sample to 873 K. Finally, upon heating to 923 K, the bubbles coalesced forming a channel of helium gas along the random grain boundary. No helium bubbles were seen at the twin boundary during this heating experiment.

The microstructural changes of the random grain boundaries after heating to 823 K and 973 K

are shown in Fig. 3(a) and (b), respectively. Similar to the previous results, many tiny helium bubbles formed along the grain boundary at 823 K. In contrast, it was difficult to see the individual helium bubbles along the grain boundary after heating to 973 K. Moreover, a jagged, brighter contrast area appeared along the grain boundary with a width of a few tens of nanometers. This contrast change is caused by the coalescence and rupture of the helium bubbles at the grain boundary.

The surface morphologies of the helium ion implanted sample after heating to 973 K were investigated by SEM. Fig. 4(a) shows the SEM image of the implanted surface including a random grain boundary. It is clear that continuous cracking has been caused along the grain boundary. The width of the crack is about 20 to 30 nm, which is almost equal to the width of the jagged, brighter contrast area in Fig. 3(b). Therefore, we deduce that the cause of the surface cracking is the formation and rupture of the helium bubbles at the grain boundary during the heating. The SEM image of an area including a faceted $\Sigma 3$ CSL boundary is shown in Fig. 4(b). No crack generation is apparent along the $\{111\}$ $\Sigma 3$ CSL (twin) boundary because the helium bubbles never nucleate on the twin boundary during heating, as indicated in Fig. 2. Conversely, discontinuous surface cracking occurred along the asymmetrical $\Sigma 3$ CSL boundary, which consisted of two connected parallel twin boundaries. This result indicates that the resistance of CSL boundaries to helium cracking depends not only on the Σ values but also on the type of boundaries involved, such as tilt or twist, symmetric

or asymmetric, etc. In other words, the behavior of the helium cracking will differ between individual CSL boundaries although they have the same Σ value.

In Fig. 5, the SEM images of two different $\Sigma 9$ CSL boundaries are presented. Surface cracking along the CSL boundaries is apparent in both images; however the nature of the cracking differs slightly. In Fig. 5(a), continuous cracking is visible at the straight $\Sigma 9$ CSL boundary, as was observed at the random grain boundary. For another $\Sigma 9$ CSL boundary with a faceted structure, as seen in Fig. 5(b), helium cracking was significantly suppressed on one facet plane (indicated by the white arrows). Thus, discontinuous cracking occurred at the faceted $\Sigma 9$ CSL boundary, similar to that observed at the $\Sigma 3$ CSL boundary.

It is expected that high resistance to helium cracking is prevalent only at some particular CSL boundaries. To characterize the nature of each $\Sigma 9$ CSL boundary, TEM samples were picked up from the area enclosed in the white, rectangular box shown in Fig. 5. Fig. 6 shows the TEM micrograph and the corresponding diffraction pattern of the sample including the straight $\Sigma 9$ CSL boundary, as shown in Fig. 5(a). The incident direction of the electron beam was parallel to the common $\langle 110 \rangle$ direction. The misorientation angle between the two grains was measured to be 37.7° . This angle is slightly different from the exact CSL relationship with a 38.9° misorientation, but the deviation of the angle is within the range of Brandon's criterion ($\Delta\theta = 5^\circ$ for $\Sigma 9$ CSL) [25]. From the TEM image, the finite width of the CSL boundary indicates that the boundary plane inclines in a different

direction from the common $\langle 110 \rangle$ direction. This implies that the CSL boundary has both the tilt and twist components for the present misorientation. Additional TEM results for the non-cracking $\Sigma 9$ CSL boundary are summarized in Fig. 7. The incident direction of the electron beam was parallel to the common $\langle 110 \rangle$ direction and the misorientation angle between the two grains was measured to be 38.7° , which is almost equal in value to the exact CSL misorientation angle. In contrast to the previous results, the CSL boundary plane seems to be exactly parallel to the electron beam direction. Therefore, this CSL boundary is classified as a pure tilt grain boundary without any twist component. The CSL boundary was indexed as the (557) and (771) lattice planes for each grain.

4. Discussion

After annealing of the helium ion implanted 316L stainless steel in the MBHVEM, surface cracking occurred along the random boundary and some CSL boundaries. This is due to the formation and rupture of helium bubbles at the grain boundaries. Helium cracking is known to occur during welding of stainless steel containing helium atoms. In the heat-up period of welding, helium bubbles nucleate at grain boundaries and grow by thermal vacancy absorption because of helium gas overpressure in the bubbles [26]. In the cooling period, the helium bubbles continuously grow by stress-induced vacancy absorption [26] due to the tensile stress associated with the solidification of the melting zone. When the tensile stress exceeds the fracture stress of the grain boundary decorated

by the helium bubbles, surface cracking occurs. It was observed that many helium bubbles nucleated and grew at the grain boundaries during *in-situ* annealing in the MBHVEM, analogous to the heat-up process during welding. However, in our experiment, the cooling rate of the sample was about 10 K/s, which is much slower than that during welding. Furthermore, there was no melting zone near the grain boundaries, hence the effect of external tensile stress can be neglected. As shown in Fig. 1, the distribution of implanted helium atoms is limited to a depth of 300 nm from the surface, resulting in helium bubbles only being nucleated at grain boundaries near the surface. When the helium bubbles grow through the absorption of both thermal vacancies and helium atoms, tensile stress is applied near the surface due to the helium gas overpressure in the bubbles (see Fig. 8). We believe that the surface cracking occurred during the annealing period in the MBHVEM (not during the cooling period) and the surface does not affect the nucleation of helium bubbles at the grain boundaries.

At the faceted CSL boundary, cracking of the surface was observed only on one boundary facet plane, whereas the other facet plane showed high resistance to helium cracking. The faceting of a grain boundary occurs in order to reduce the total grain boundary energy despite causing an increase in the total area of the grain boundary. It is therefore necessary that the grain boundary energy of at least one facet plane is less than the grain boundary energy before faceting. Nucleation of helium bubbles is suppressed at the lower energy boundary. This is the reason why discontinuous cracking is

observed on the faceted CSL boundaries. For example, the $\{111\}$ $\Sigma 3$ CSL boundary (twin boundary) is one of the special boundaries which has a very low energy compared with the other grain boundaries [27], such that a $\Sigma 3$ CSL boundary is always faceted into the twin boundary and another $\Sigma 3$ CSL boundary. Actually, our TEM and SEM observations showed that the formation and rupture of the helium bubbles was perfectly restricted to the twin boundary facet because of its low boundary energy.

At the faceted $\Sigma 9$ CSL boundary, surface cracking occurred on one boundary facet having both the tilt and twist components, whereas no crack formed on another facet having a pure tilt boundary. This implies that the pure tilt boundary is one of the lower energy boundaries in the $\Sigma 9$ CSL relationship. With respect to the CSL theory, it has been considered that asymmetrical tilt CSL boundaries have higher boundary energies than symmetrical tilt CSL boundaries because they contain fewer CSL sites [28]. However, recent study shows that the asymmetrical tilt boundary energy weakly depends on the inclination angle in copper and the absolute energies of the asymmetrical $\Sigma 9$ CSL tilt boundary are within the range of the energies of two symmetrical $\Sigma 9$ CSL tilt boundaries [29]. On the other hand, the energy difference between the tilt and twist boundaries has been investigated theoretically in detail by Wolf [30-33]. It was found that, in general, the energy of the general boundaries is higher than that of the tilt boundaries in certain CSL relationships. It is therefore expected that the boundary energy of two facets in the $\Sigma 9$ CSL boundary is different each

other; the pure tilt boundary facet always has a lower boundary energy than that in another boundary facet having both the tilt and twist components. In fact, the cracked $\Sigma 9$ CSL boundaries always had a twist component. At the $\Sigma 9$ CSL boundaries, we can conclude that surface cracking is suppressed on the pure tilt boundary facet because of its low boundary energy. Further TEM analysis for the other faceted $\Sigma 9$ CSL boundaries will be required to confirm the above result. The grain boundary energy estimation based on the atomistic simulation will also help us to understand the effect of the index of the boundary planes.

5. Conclusions

The nucleation and growth of helium bubbles on a random grain boundary in helium ion implanted 316L stainless steel was observed during annealing up to 973 K. After annealing, surface cracking occurred on random grain boundaries and some CSL boundaries due to the formation and rupture of helium bubbles at the grain boundaries. At the faceted CSL boundaries, surface cracking occurred only on one boundary facet plane, whereas no crack was observed on the other facet plane. It was shown that the twin boundary has the highest resistance to helium cracking at the $\Sigma 3$ CSL boundaries. At the $\Sigma 9$ CSL boundaries, the pure tilt boundary shows high resistance to cracking because of its low boundary energy. It is suggested that the propagation of helium cracking can presumably be prevented in the austenitic stainless steel having high density $\Sigma 3$ and $\Sigma 9$ CSL

boundaries.

Acknowledgements

The authors gratefully thank Mr. K. Sugawara and Mr. K. Ohkubo for their technical support in the MBHVEM operations.

References

- [1] P. L. Lane, P. J. Goodhew, J. Nucl. Mater. 122&123 (1984) 509-513.
- [2] H. Schroeder, N. Yamamoto, J. Nucl. Mater. 179-181 (1991) 453-456.
- [3] N. Yamamoto, T. Chuto, Y. Murase, J. Nagakawa, J. Nucl. Mater. 329-333 (2004) 993-997.
- [4] A. Leeser, H. Ullmaier, J. Nucl. Mater. 155-157 (1988) 968-972.
- [5] N. Kishimoto, R.E. Clausing, L. Heatherly, Jr., K. Farrell, J. Nucl. Mater. 179-181 (1991) 998-1002.
- [6] H. T. Lin, B. A. Chin, J. Mater. Sci. 26 (1991) 2063-2070.
- [7] C. A. Wang, M. L. Grossbeck, B. A. Chin, J. Nucl. Mater. 225 (1995) 59-68.
- [8] K. Watanabe, S. Jitsukawa, S. Hamada, T. Kodaira, A. Hishinuma, Fusion Eng. Des. 31 (1996) 9-15.
- [9] D. N. Braski, H. Schroeder, H. Ullmaier, J. Nucl. Mater. 83 (1979) 265-277.

- [10] S. Kawano, R. Sumiya, K. Fukuya, J. Nucl. Mater. 258-263 (1998) 2008-2012.
- [11] Y. Pan, B. L. Adams, T. Olson, N. Panayotou, Acta Mater. 44 (1996) 4685-4695.
- [12] T. Watanabe, M. Yamada, S. Karashima, Phil. Mag. A 63 (1991) 1013-1022.
- [13] N. Sakaguchi, S. Watanabe, H. Takahashi, R. G. Faulkner, J. Nucl. Mater. 329-333 (2004) 1166-1169.
- [14] Y. Zhou, K.T. Aust, U. Erb, G. Palumbo, Scrip. Mater. 45 (2001) 49-54.
- [15] G. Palumbo, K. T. Aust, Acta Metall. Mater. 38 (1990) 2343-2352.
- [16] P. Lin, G. Palumbo, U. Erb, K. T. Aust, Scrip. Metall. Mater. 33 (1995) 1387-1392.
- [17] C. Cheung, U. Erb, G. Palumbo, Mater. Sci. Eng. A 185 (1994) 39-43.
- [18] E.M. Lehockey, G. Palumbo, Mater. Sci. Eng. A 237 (1997) 168-172.
- [19] G. Palumbo, E.M. Lehockey, P.Lin, JOM. 50 (1998) 40-43.
- [20] E.M. Lehockey, G. Palumbo, P. Lin, Scripta Mater. 36 (1997) 1211-1218.
- [21] G. Palumbo, U.Erb, MRS. Bul. 24 (1999) 27-32.
- [22] S. Spigarelli, M. Cabibbo, E. Evangelista, G. Palumbo, Mater. Sci. Eng. A. 352 (2003) 93-99.
- [23] M. Michiuchi, H. Kokawa, Z.J. Wang, Y.S. Sato, K. Sakai, Acta Mater. 54 (2006) 5179-5184.
- [24] <http://www.srim.org/>
- [25] D.G. Brandon, Acta Metall. 14 (1966) 1479-1484.
- [26] H. T. Lin, M.L. Grossbeck, B.A. Chin, Metall. Trans. 21A (1990), 2585-2596.

[27] D. L. Olmsted, S. M. Foiles, E. A. Holm, *Acta Mater.* 57 (2009) 3694-3703.

[28] D.G. Brandon, *Acta Metall.* 14 (1966) 1479-1484.

[29] N. Gokan, M. Kajihara, *Mater. Sci. Eng. A* 477 (2008) 121-128.

[30] D. Wolf, *Acta. Metall.* 37 (1989) 1983-1993.

[31] D. Wolf, *Acta. Metall.* 37 (1989) 2823-2833.

[32] D. Wolf, *Acta. Metall.* 38 (1990) 781-790.

[33] D. Wolf, *Acta. Metall.* 38 (1990) 791-798.

Figure and table captions:

Table 1. Bulk composition of the 316L austenitic stainless steel given in mass percent.

Fig.1 Implanted helium concentration profile as a function of depth, calculated by SRIM software [24].

Fig.2 Behavior of helium bubble nucleation and growth on a random grain boundary during *in-situ* annealing in the MBHVEM up to 923 K.

Fig.3 TEM micrographs of random grain boundaries in helium implanted 316L stainless steel after annealing at (a) 823 K and (b) 973 K for 45 minutes.

Fig.4 SEM images of surface cracking on (a) the random grain boundary and (b) the $\Sigma 3$ CSL boundary in helium implanted 316L stainless steel after annealing at 973 K for 45 minutes.

Fig. 5 SEM images of surface cracking on (a) the straight $\Sigma 9$ CSL boundary and (b) the faceted $\Sigma 9$ CSL boundary in helium implanted 316L stainless steel after annealing at 973 K for 45 minutes.

Fig.6 TEM micrograph of a cracked $\Sigma 9$ CSL boundary and the corresponding diffraction pattern from the sample picked up using the FIB technique from the area enclosed in the white rectangular box in Fig. 5(a).

Fig.7 TEM micrograph of a non-cracked $\Sigma 9$ CSL boundary and the corresponding diffraction pattern from a sample picked up using the FIB technique from the area enclosed in the white rectangular box in Fig. 5(b).

Fig.8 Schematic illustration of the generation of surface stress caused by helium bubble overpressure formed on the grain boundary near the surface.

Table 1

	C	Si	Mn	P	S	Ni	Cr	Mo	Fe
mass%	0.01	0.59	0.78	0.033	0.001	12.16	17.22	2.06	Bal.

Fig.1

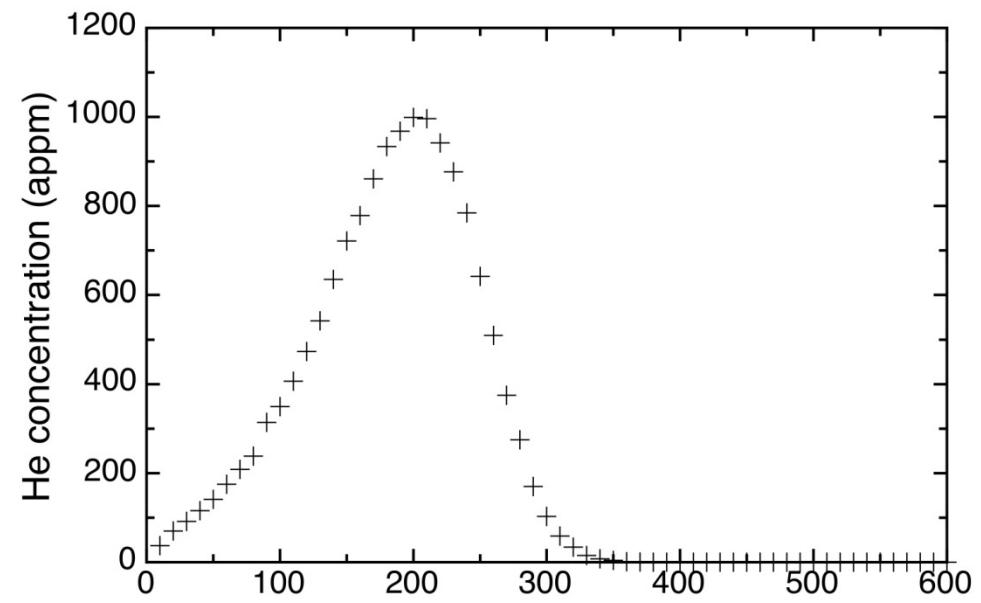
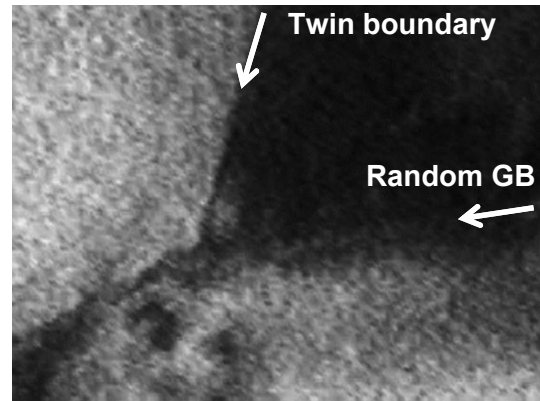


Fig.2

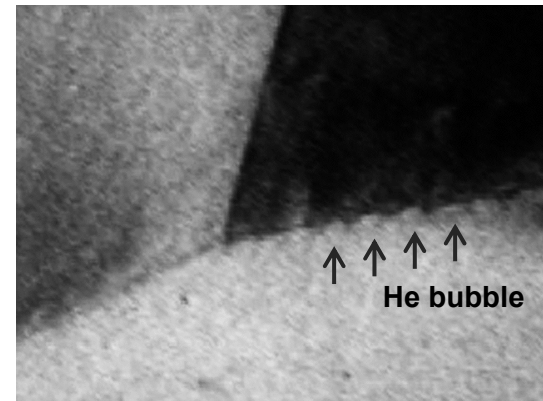
293K



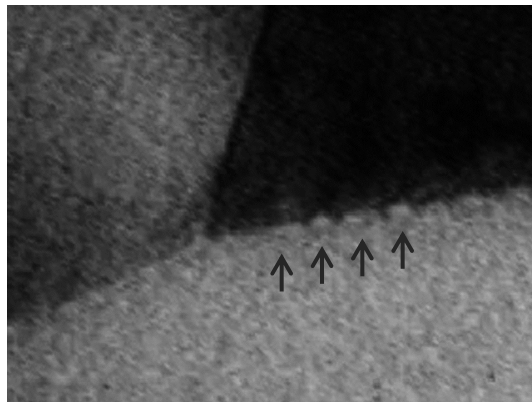
723K



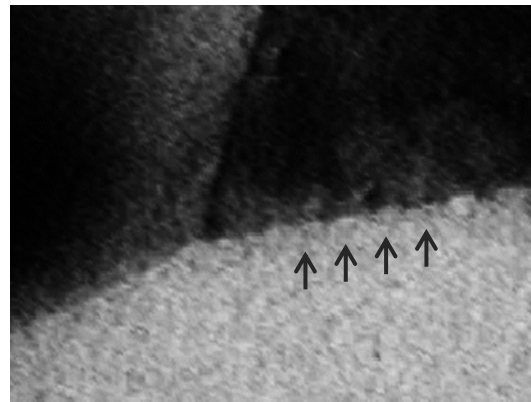
773K



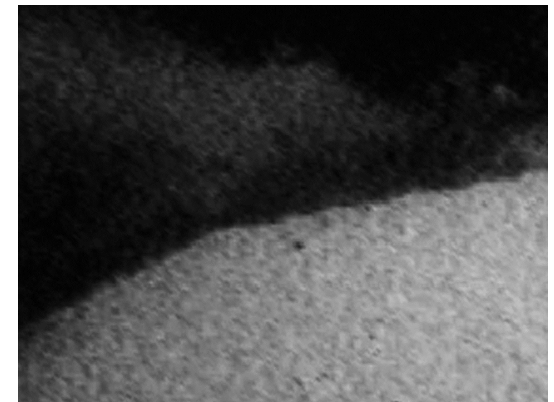
823K



873K

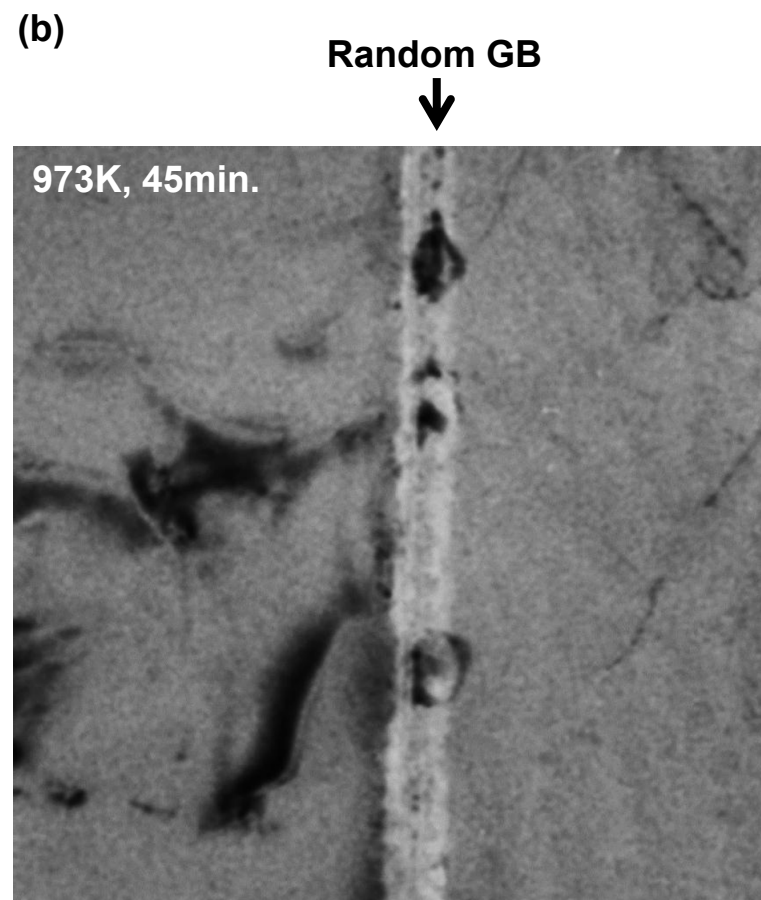
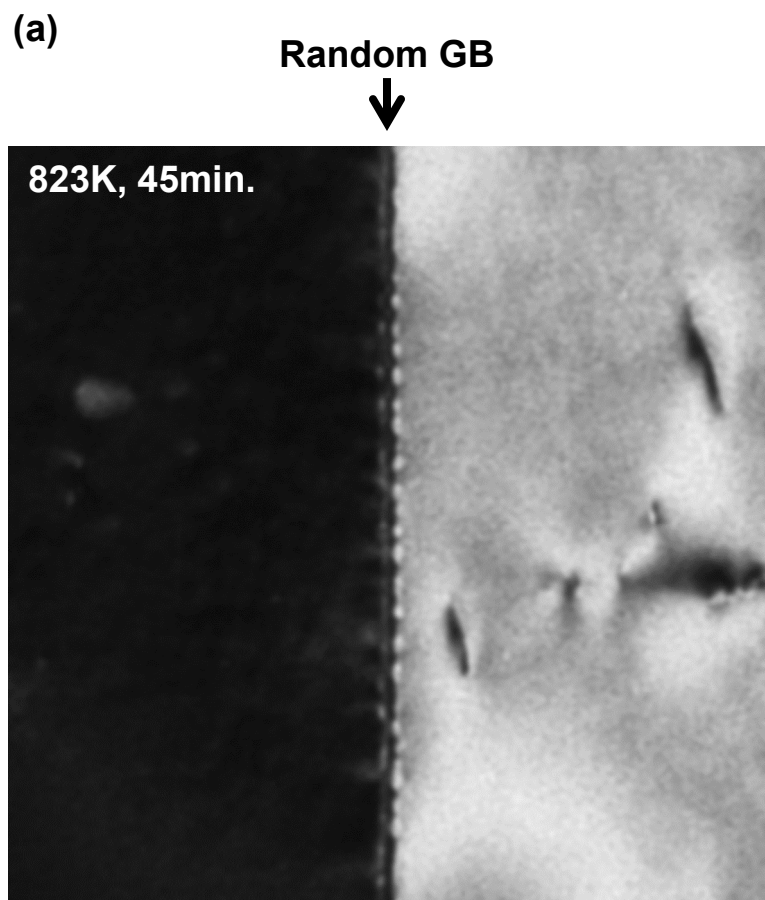


923K



50nm

Fig.3



200nm

Fig.4

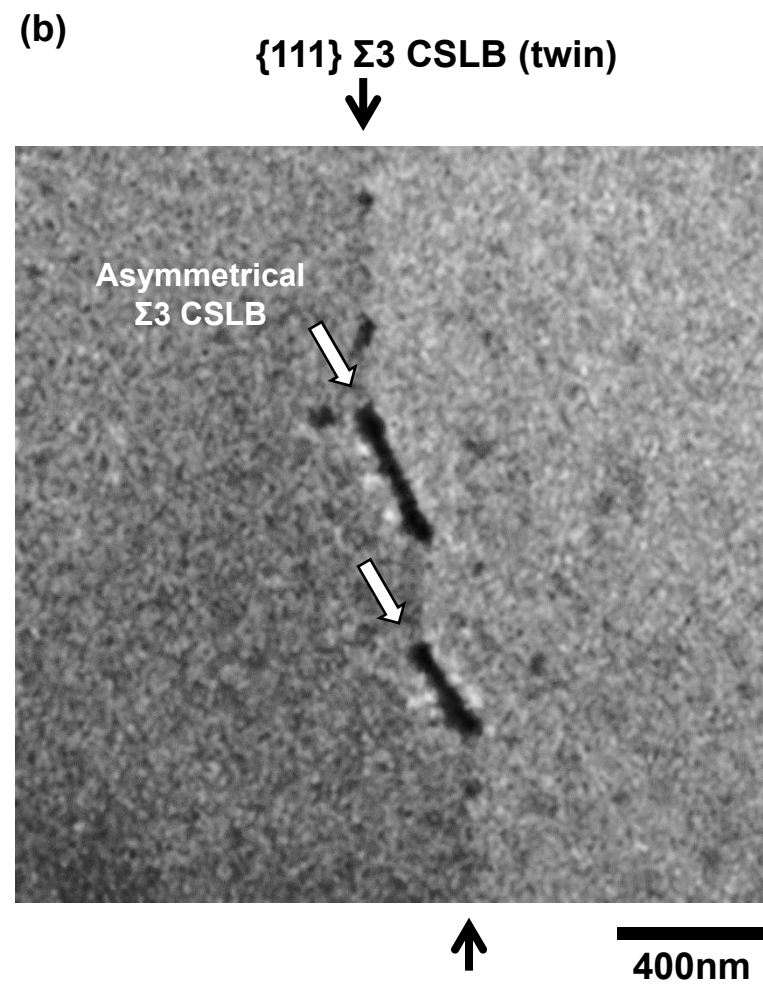
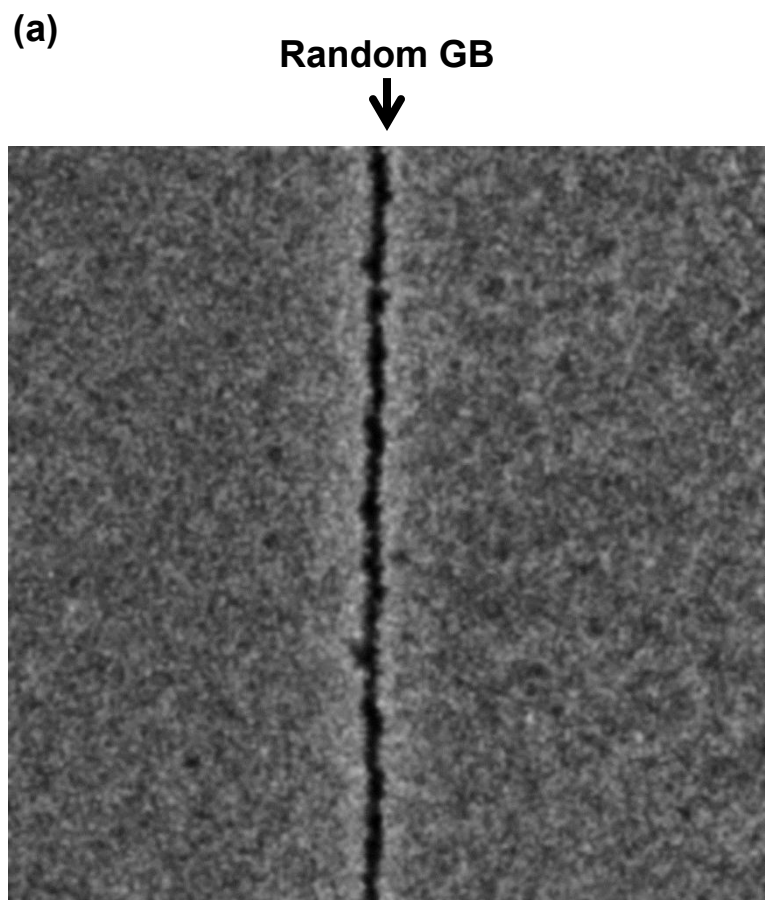
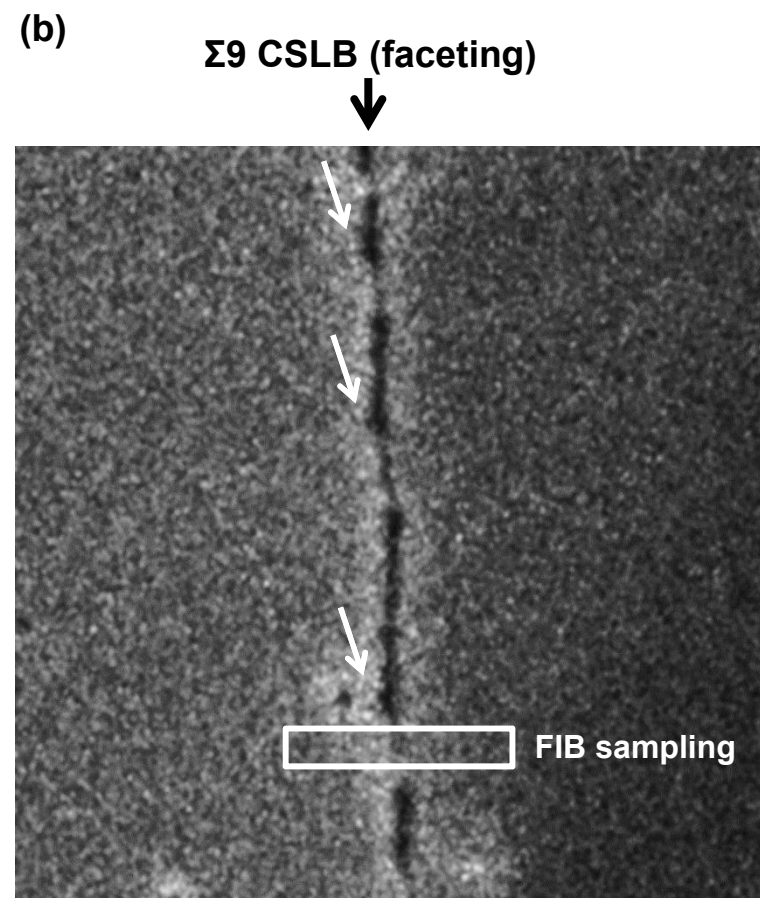
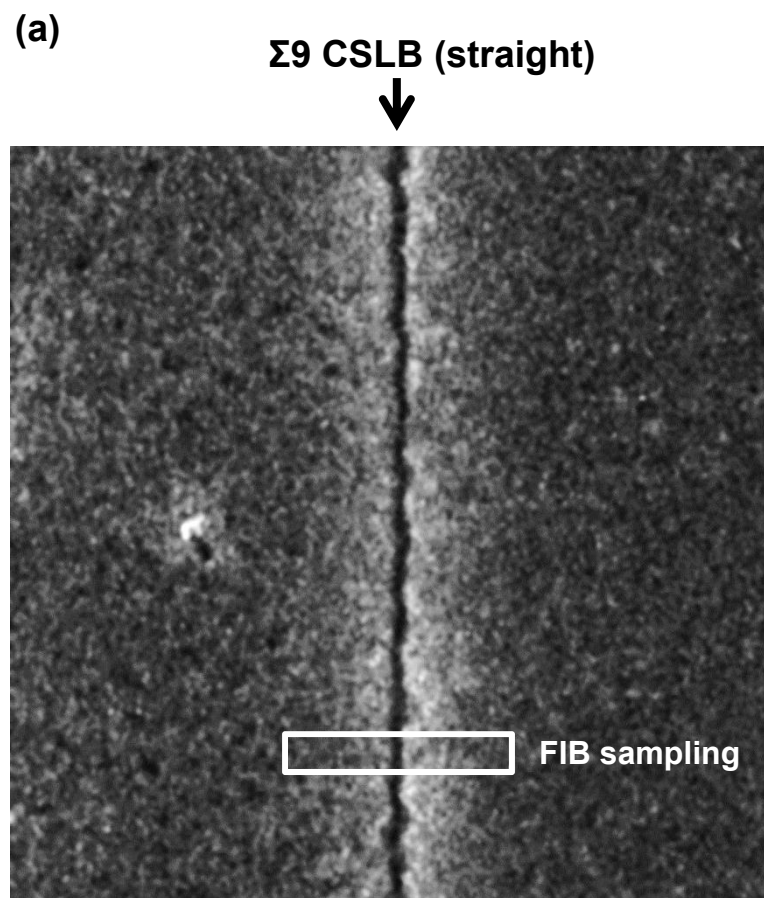


Fig.5



400nm

Fig.6

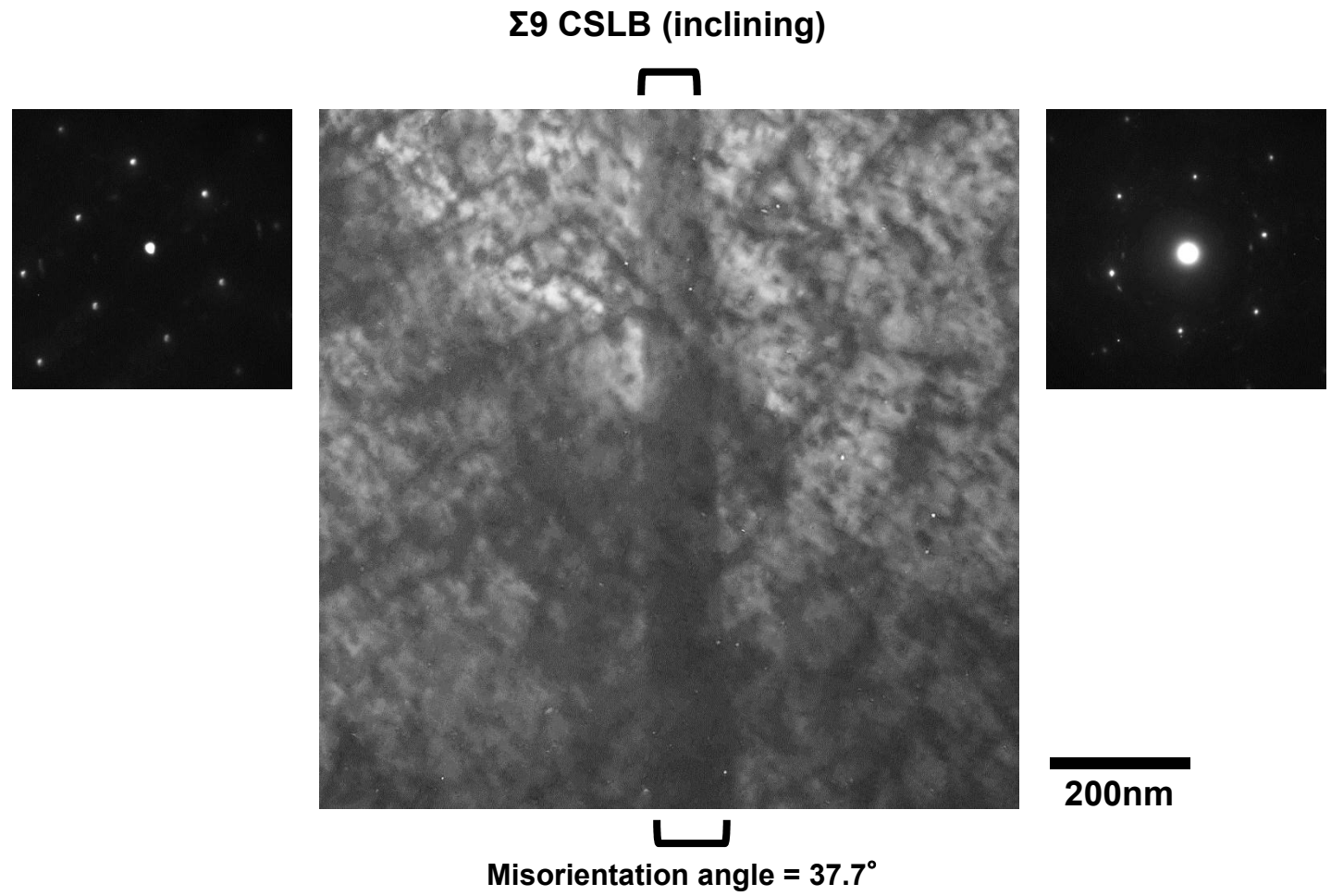


Fig.7

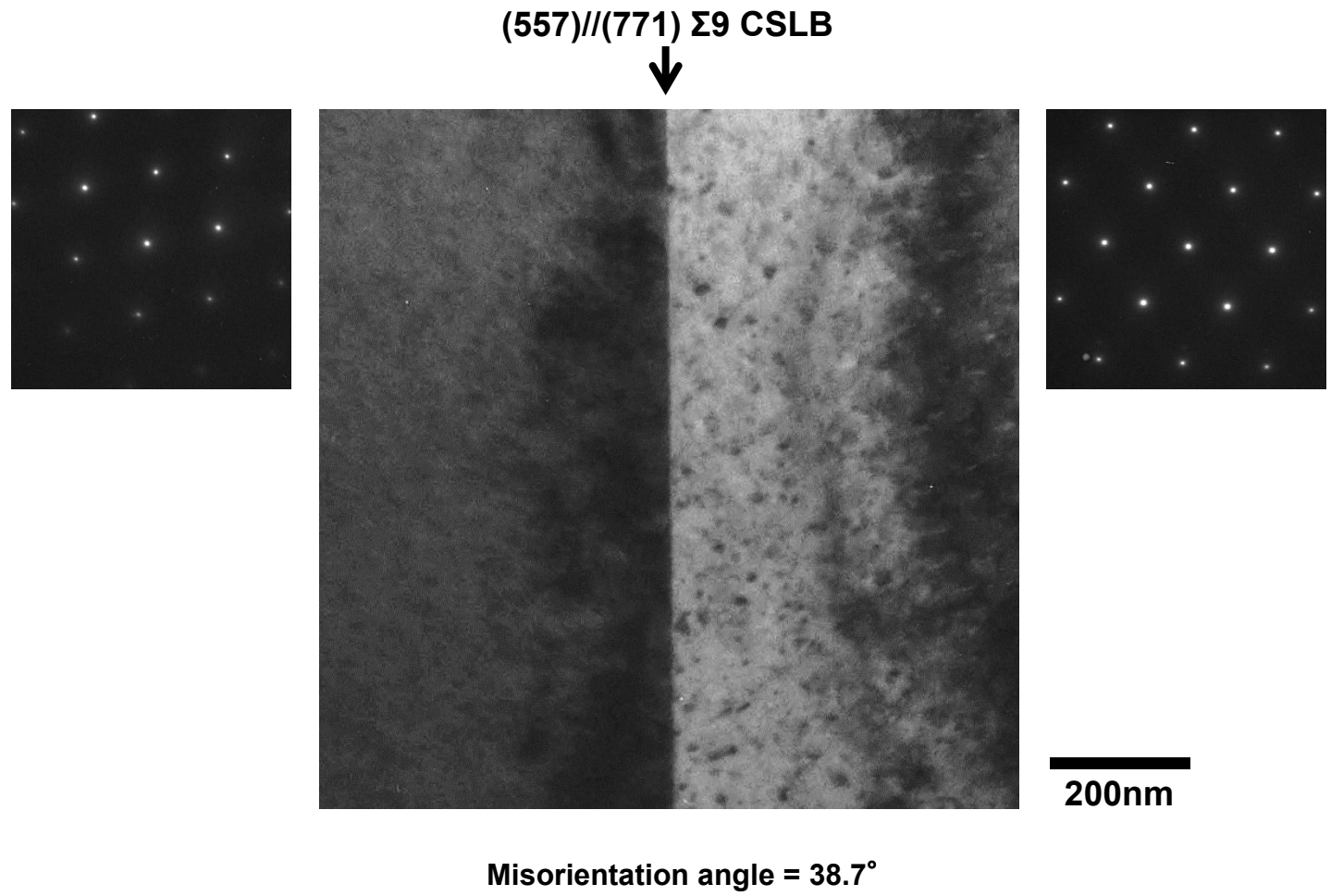


Fig.8

